Effects of the oxygen source configuration on the superconducting properties of internally-oxidized internal-Sn Nb$_3$Sn wires

G Bovone[1,*] ⓘ**, F Buta**[1] ⓘ**, F Lonardo**[1]**, T Bagni**[1] ⓘ**, M Bonura**[1] ⓘ**, D LeBoeuf**[2]**,**
S C Hopkins[3]**, T Boutboul**[3]**, A Ballarino**[3] **and C Senatore**[1] ⓘ

[1] University of Geneva, DQMP, Geneva, Switzerland
[2] Laboratoire National des Champs Magnétiques Intenses, Grenoble, France
[3] European Organization for Nuclear Research CERN, Geneva, Switzerland

E-mail: gianmarco.bovone@unige.ch

CrossMark

Abstract

We successfully manufactured 12-filament rod-in-tube Nb$_3$Sn wires with oxide nanoparticles formed by the internal oxidation method. We employed Nb-7.5 wt%Ta-1 wt%Zr and Nb-7.5 wt%Ta-2 wt% Hf alloys along with oxygen sources (OSs) in two different configurations—in the core of Nb filaments (coreOS) and at the boundary between the filaments and the Cu tube (annularOS)—to assess the influence of the OS layout on the superconducting properties and grain size. The simultaneous presence of the OS and of Hf or Zr reduced the average Nb$_3$Sn grain size to around 50 nm, leading to an enhancement of the layer critical current density (J_c) up to 3000 A mm^{-2} at 4.2 K and 16 T for the Hf-annularOS wire. Samples manufactured with an OS show a shift toward higher reduced magnetic fields of the position of the maximum in pinning-force density, this shift being more pronounced when SnO$_2$ is added in the annularOS configuration, and for the Hf-containing samples. This enhanced pinning at higher magnetic field is beneficial for high-field magnet applications. Moreover, we measured a very high upper critical field, reaching 29.3 T at 4.2 K in the Hf-annularOS samples.

Keywords: Nb$_3$Sn, internal oxidation, multi-filamentary wire

(Some figures may appear in colour only in the online journal)

1. Introduction

Nb$_3$Sn superconductor is currently the preferred solution for the conductor of the next generation of high field accelerator magnets. An example is the High Luminosity upgrade of the Large Hadron Collider (HL-LHC) [1] at the European Organization for Nuclear Research (CERN). One of the objectives of this program is the installation in the interaction region of high-field large-aperture Nb$_3$Sn quadrupole magnets, with a peak field on the conductor of 12 T [2]. This goal required the development of Nb$_3$Sn wires with a non-Cu J_c (i.e., the critical current, I_c, divided by the wire's non-Cu area, including Nb$_3$Sn, residual bronze, and barriers) of 2450 A mm^{-2} at 4.2 K and 12 T. CERN is undertaking a study for a new proton-proton collider known as the future circular collider (FCC-hh) [3], a $\sim$100 km circumference ring with 16 T Nb$_3$Sn dipole magnets, and a resulting collision energy

of 100 TeV. The need of reaching a dipole field of 16 T in a compact and economically viable magnet translates into a non-Cu J_c target for the Nb_3Sn wires of 1500 A mm^{-2} at 4.2 K and 16 T [4]. For comparison, under the same conditions, the wires developed for the HL-LHC upgrade can exhibit a non-Cu J_c value as high as 1250 A mm^{-2} at 4.2 K and 16 T [5, 6].

Progress in wire technology continuously improved the critical current density (layer J_c, i.e., the I_c divided by the Nb_3Sn area) until the early 2000s [7], when internal Sn multi-filamentary wires were optimized using the Rod-Restack-Process (RRP®) [8]. The RRP® is a rod-in-tube (RIT) technique that involves stacking hundreds of Nb filaments jacketed in Cu around a sacrificial Cu core that is subsequently replaced with a Sn rod to form a sub-element, which is later cut and restacked to create the multi-filamentary wire. A heat treatment at temperatures ranging from 640 °C to 700 °C is then needed to form the Nb_3Sn phase. In inclusion-free Nb3Sn the grain boundaries are the main pinning centers; therefore, materials with finer grains have higher current densities. In highly optimized RIT wires, Nb3Sn typically has grain sizes of ∼100–150 nm [9]. Tailoring the heat treatment to promote the Sn diffusion and introducing proper amounts of Ti or Ta, it is possible to achieve non-Cu J_c values of 1200 A mm^{-2} at 16 T and 4.2 K, whereas the fine tuning of the Cu to Nb local area ratio and the overall Nb content of the subelements [10] led to 1300 A mm^{-2} (16 T, 4.2 K). These values are still 13%–20% lower than the FCC target [11]. Barzi *et al* [10] clearly concluded that the J_c of the RRP® wires has plateaued and that further efforts should concentrate on improving the inherent pinning of these wires. Similar considerations apply to the wires produced by the powder-in-tube (PIT) route [12], with the highest non-Cu J_c reported in the literature being close to 1300 A mm^{-2} (16 T, 4.2 K) [13]. For the dependence of pinning force on grain size reported in the literature [14, 15], we can estimate that a reduction in the grain size down to 50–60 nm would effectively enhance the non-Cu J_c beyond the FCC specification.

Investigations on practical methods for inhibiting the grain growth in Nb_3Sn date back to the 1960s when the first evidence of Nb_3Sn grain refinement due to grain growth inhibition was observed by Benz [16]. A Nb-1%Zr tape was anodized and heat-treated to introduce oxygen in the Nb matrix. The resulting tape was then coated with Sn and heated above 930 °C to form a layer of Nb_3Sn at the interface. The presence of ZrO_2, formed by the internal oxidation of Zr in the alloy, inhibited the grain growth of Nb_3Sn. In composite multi-filamentary wires, adopting a similar approach is unfeasible because Nb filaments are embedded in a Cu or bronze matrix to lower the formation temperature of Nb_3Sn. Oxygen cannot readily diffuse into Nb from the outside at the end of the deformation process, and introducing oxygen into Nb beforehand would considerably increase its hardness and reduce deformability. The other possibility is to supply oxygen from a judiciously placed separate oxygen source (OS) from which oxygen can effectively diffuse through the Nb alloy after the deformation process (i.e. during heat treatment). Zeitlin *et al* [17] were the first to report an attempt to inhibit grain growth in a round-wire conductor by the addition of an OS. This was done in RIT type

wires based on Nb-1%Zr filaments whose solid Sn core was replaced by a mixture of Sn and SnO_2 powders. SnO_2 was supposed to decompose during the heat treatment and, after diffusion through the Cu and the Nb alloy, react with Zr (owing to its higher affinity for oxygen), forming ZrO_2 to inhibit grain growth. The reacted wire displayed no signs of grain refinement at the usual Nb_3Sn reaction heat treatment temperatures, presumably because of the Cu separating the Sn core from the filaments.

In 2014, Xu *et al* [18] demonstrated the feasibility of internal oxidation in a mono-filamentary tube-type wire, reporting Nb_3Sn with an average grain size of 43 nm. SnO_2 powder was added at the interface between the Nb-1%Zr tube and the internal Cu/Sn core. During heat treatment, the SnO_2 in contact with the Nb-1%Zr alloy decomposes, supplying oxygen to the alloy for the formation of ZrO_2 precipitates. The proposed mono-filamentary wire also exhibited a modified pinning mechanism, showing a shift in the maximum pinning force to higher reduced magnetic fields. At the University of Geneva, we were able to reproduce some of these results in mono-filamentary thin wires (diameter of 0.22 mm) with various Nb alloys (Nb-1 wt%Zr, Nb-7.5 wt%Ta-1 wt%Zr, Nb-7.5 wt%Ta-2 wt%Zr) and different OSs (SnO_2, CuO) that were centrally placed in the Nb alloy [19]. No pinning peak shift was observed, but samples fabricated with the Nb-7.5 wt%Ta-2 wt%Zr alloy exhibited an outstanding B_{c2} value of 29.2 T at 4.2 K [20]. Motowidlo *et al* [21] used a PIT method to fabricate multi-filamentary wires based on Nb-1 wt% Zr tubes filled with a mixture of Cu_5Sn_4 and Sn powders. A relatively large grain size gradient was observed, but the area equivalent mean diameter was as low as 30 nm at the interface with the Nb alloy. Transport measurements over a wide range of magnetic fields allowed the deconvolution of the pinning force density into grain boundary and point defect contributions, the latter being found to dominate with contributions from 65% to 76%, depending on composition and heat treatment. Balachandran *et al* [22] fabricated Nb_3Sn mono-filamentary wires based on a Nb alloy containing Hf, namely Nb-7.5 wt% Ta-1 wt% Hf. A rod of this alloy was placed in the core of the wire, surrounded by a mixture of Sn and Cu powder, and SnO_2 was added to the mixture to examine the effect of OS on different alloys. A Ta barrier was placed to hold the powder mix and prevent the contamination of the external Cu stabilizer. The use of a Hf-containing alloy without the intentional addition of OS reduced the Nb_3Sn average grain size from 107 nm (as measured on a reference Nb–Ta wire fabricated with the same architecture) to 68 nm. The wire fabricated with SnO_2 addition had a smaller grain size (55 nm) but exhibited a lower pinning force at the peak field. Banno *et al* [23] studied Nb_3Sn bulks made from Hf-containing Nb alloys, correlating the reduced Nb_3Sn grain size with the smaller grain size of the original Hf-containing Nb alloy. Grain refinement was observed in Nb_3Sn synthesized from an annealed alloy; however, the grain size of Nb_3Sn without intentional OS was reduced to 81 nm.

Xu *et al* [24] further applied the internal oxidation to powder-in-tube multi-filamentary Nb_3Sn wires based on ternary Nb alloys (Nb-7.5 wt% Ta-1 wt% Zr), with subelement numbers and wire lengths approaching those of practical

wires. To fabricate these 'additional pinning center-powder in tube' (APC-PIT) wires Cu-jacketed Nb-7.5 wt% Ta-1 wt% Zr tubes were filled with a mixture of Cu, SnO_2 and Sn powders. After the initial deformation, the resulting assemblies were cut and used as subelements in a Cu tube to prepare multi-filamentary wires. These multi-filamentary APC-PIT wires exhibited high B_{c2} owing to effective Ta doping [25], and high J_c owing to the effective ZrO_2 APC, some of them surpassing the FCC specification [26]. In other powder-in-tube multi-filamentary Nb_3Sn wires based on Nb-1 wt% Zr and SnO_2 powder as OS [27], grain refinement was not observed even though nanoscale precipitates were present and a shift of maximum pinning force density to higher magnetic field was measured. It was argued that the oxidation of Nb–Sn intermetallics deprives some of the Zr from oxygen needed for its oxidation.

In the framework of a collaboration between UNIGE and CERN, we present here the results of our investigation on internal Sn wires with an internal OS to enhance the superconducting properties of Nb_3Sn. This study explores methods to add an internal OS to a simplified RIT wire, which imitates a subelement of RIT wires with a reduced number of Nb-alloy filaments. The absence of powder in the design of current RIT wires necessitates preliminary studies to evaluate the effects of powder OS in different layouts on wire deformability/fabrication and superconducting properties. We have developed a versatile design that enables us to investigate the properties of different Nb-alloys (Nb-7.5 wt% Ta-1 wt% Zr; Nb-7.5 wt% Ta-2 wt% Hf) combined with two possible OS configurations (*annularOS* and *coreOS*) in a 12-filament arrangement surrounding a Sn core. This fast turnaround R&D activity allowed us to investigate the effects on the superconducting properties of the position of the OS relative to the Nb_3Sn formation front, as detailed below.

2. Experimental methods and details

2.1. Wire fabrication

The wires presented in this work were based on two different Nb-7.5 wt%Ta alloys, distinguished by a third element:

(1) Hf in the Nb alloy: Nb-7.5 wt%Ta-2 wt%Hf
(2) Zr in the Nb alloy: Nb-7.5 wt%Ta-1 wt%Zr.

The weight percentage of Hf was selected such as to have the same atomic fraction of Hf in the Nb–Ta–Hf alloy as of Zr in the Nb–Ta–Zr alloy, namely 1.1 atomic %.

For each of these alloys, we prepared a reference wire without an OS and two wires with different OS layouts, as illustrated in figure 1 and described here:

(a) *noOS*: without OS as reference sample for the series (figure 1(a))
(b) *coreOS*: SnO_2 was placed at the core of each Nb alloy filament (figure 1(b))
(c) *annularOS*: SnO_2 placed around each Nb-alloy filament (figure 1(c)).

We additionally manufactured a wire using a Nb-7.5 wt%Ta alloy, without OS, used as a reference sample for comparison (NbTa-*noOS*). Table 1 provides a summary of the manufactured wires with the alloy used for the filaments and OS layout.

To prepare the filaments of the *coreOS* wires, a central hole was drilled in the Nb alloy and filled with SnO_2 powder (Inframat Advanced Materials, 80 nm nominal particle size) at tap density. The hole was sized to accommodate enough OS to supply the oxygen necessary for oxidizing all the Hf or Zr atoms in the Nb alloy, assuming a 50% packing density of the oxide powder.

For the *annularOS* technique, we coated the Nb alloy filaments with a thin layer of SnO_2 by dip coating [28]. Colloidal solutions of the SnO_2 (30 wt%) in ethanol were prepared, and included polyvinyl butyrate (PVB, 2 wt%) to reduce the formation of cracks in the coated layer during the evaporation of the ethanol. The Nb alloy rods were dipped into the suspension and air-dried for 10 min. This process was repeated until the deposited SnO_2 (evaluated by weighing the dried rod) was sufficient to provide the amount of oxygen required to oxidize all Hf or Zr atoms in the Nb alloy.

The Cu/Nb filaments were assembled by inserting a 4.9 mm Nb alloy rod (with or without an OS) into a Cu tube (outer diameter, OD = 6.30 mm; inner diameter, ID = 5.30 mm). The assembly was cold-deformed by swaging and wire drawing to a diameter of 1.12 mm. For reasons related to the co-deformation of the Cu/Nb assembly, we used an excess of Cu relative to the desired Cu-to-filament area ratio of 0.2. After the deformation process, electropolishing [29] was employed to remove excess Cu from the Cu/Nb filaments.

The Cu/Sn rod was directly assembled with the intended Cu-to-filament area ratio of 0.2.

Twelve Cu/Nb filaments and a central Cu-clad Sn rod were inserted inside a Ta tube, which acts as a barrier to preserve the purity of the external Cu stabilizer. The surfaces of all the filaments and tubes were mechanically and chemically cleaned before assembly. The assemblies were then swaged and drawn to achieve a final diameter of 0.70 mm.

After cleaning, straight samples (16 cm in length) with hammered ends (to minimize Sn leakage) were inserted into quartz tubes and heat treated under vacuum at 650 °C for 200 h, with an intermediate plateau at 550 °C for 100 h. This plateau at 550 °C is thought to facilitate oxygen diffusion into the Nb alloy before the formation of Nb_3Sn, as also used in [22].

2.2. Characterization techniques

After deformation, we cut short wire pieces to examine the cross-section of the deformed wire and assess the filament homogeneity using scanning electron microscopy (SEM) images taken with a JEOL JSM-7600F field emission scanning electron microscope (FESEM). For each filament in a wire cross-section, we measured the average of four diameters along four different directions. Taking into account all 12 filaments, we calculated the mean average filament size for each wire and its standard deviation. Moreover, we measured the
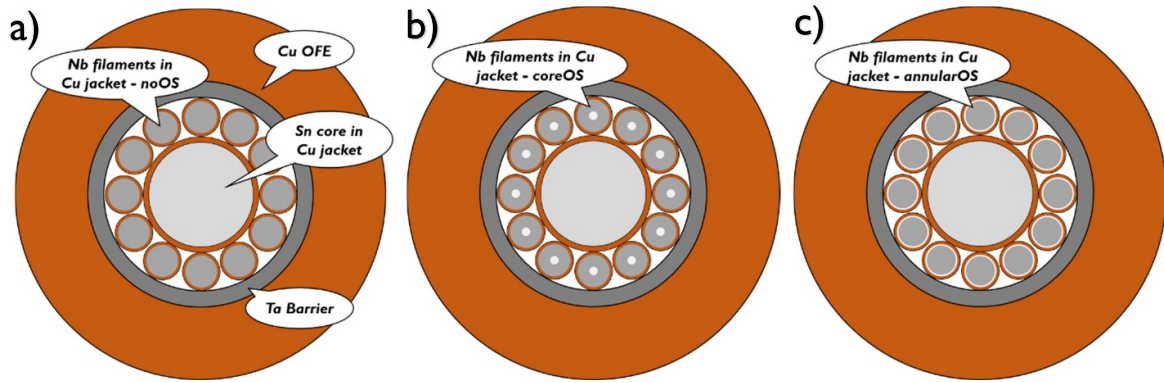
Figure 1. Rod-in-tube design for the wires reported in the paper and comparison between SnO_2 layouts: (a) no addition of SnO_2 (*noOS*), (b) SnO_2 added in the Nb filament core (*coreOS*), or (c) SnO_2 at the interface between Nb filaments and Cu jacket (*annularOS*).

Table 1. List of wire types and their filament alloy and oxygen source configuration. All percentages are by weight.

Wire type ID	Alloy in the Cu/Nb filaments (wt%)	Oxygen source material	Oxygen source position
NbTa-*noOS*	Nb-7.5%Ta	No oxide	N.A.
Hf-*noOS*	Nb-7.5%Ta-2%Hf	No oxide	N.A.
Hf-*coreOS*	Nb-7.5%Ta-2%Hf	SnO_2	Core
Hf-*annularOS*	Nb-7.5%Ta-2%Hf	SnO_2	Annular
Zr-*noOS*	Nb-7.5%Ta-1%Zr	No oxide	N.A.
Zr-*coreOS*	Nb-7.5%Ta-1%Zr	SnO_2	Core
Zr-*annularOS*	Nb-7.5%Ta-1%Zr	SnO_2	Annular

areas and elemental area ratios of Cu, Nb, and Sn enclosed by the barrier (excluding external stabilizer Cu and barrier).

Following the heat-treatment, we examined fractured cross-sections of the wires to determine the average grain size following the line intercept method. As also observed in our previous work [20], wires containing an OS exhibited elongated Nb_3Sn grains, so we evaluated the grain size in both the long- and short-axis directions. We determined the intercept distances of two lines for each axis direction. This was repeated on multiple images (from 5 to 10) for each wire to calculate the mean intercept distance (as an arithmetic mean) and its standard deviation.

Polished cross-sections were examined using the FESEM to determine the thickness and the area of the fine Nb_3Sn grain region. We calculated the thickness as the arithmetic mean over multiple values of the thickness of the fine-grained Nb_3Sn area. For each reacted filament we measured the length of four diameters along four different directions to calculate the outer (D) and inner diameter (d) of the fine-grained area. The difference divided by two was used to calculate the average layer thickness. The area of fine Nb_3Sn grains was measured on the wire samples subjected to transport critical current (I_c) measurement.

I_c measurements were performed at 4.2 K in magnetic fields of up to 19 T at the University of Geneva. The samples were 50 mm long, with two sets of voltage taps placed at distances of ∼20 and ∼10 mm. The criterion for the critical current determination was 0.1 μV cm^{-1}. The layer J_c was calculated by dividing I_c by the transverse area of fine-grained Nb_3Sn. The determination of I_c was only possible down to 10–12 T, due to the presence of electromagnetic and thermal instabilities at

lower fields. As a complement, the layer J_c was extracted using equation (1) from the $M(H)$ loops acquired in a temperature range from 4.2 to 16 K and in magnetic fields up to 7 T using a VSM SQUID. The formula is an application of Bean's critical state model [30] to a hollow cylinder [31, 32] with its axis perpendicular to the magnetic field [33]:

$$J_{c,\text{layer}} = \frac{30\pi}{4} \times \frac{1}{1 - \left(\frac{d}{D}\right)^3} \times \frac{\Delta M}{D}. \tag{1}$$

The opening (ΔM) of the $M(H)$ loop in the magnetic field of interest was measured in emu cm^{-3}. D and d represent the outer and inner diameters (cm) of the fine-grained area of the superconductor in the shape of a hollow cylinder, respectively. The values of J_c (B, T) were used to calculate the pinning force ($F_p = J_c \times B$).

We determined the B_{c2} as a function of temperature using low-current four-point transport measurements in magnetic fields up to 35 T at the Laboratoire National des Champs Magnétiques Intenses (LNCMI) in Grenoble, France, on a specially designed four-sample probe [34]. The samples were probed with a current between 1 and 5 mA, equivalent to a current density in the superconductor in the range of 0.1–0.5 A mm^{-2}. The upper critical field was extracted from the $R(B)$ curves using different criteria (99%, 90%, 50%, 10%, and 1%). For most samples, the outer Cu was chemically removed to expose the Ta barrier, which increased the electric resistance of the samples and enhanced the signal-to-noise ratio. Several wire samples were measured both with and without external Cu, demonstrating a negligible effect of precompression on B_{c2} on the wires manufactured for this work.
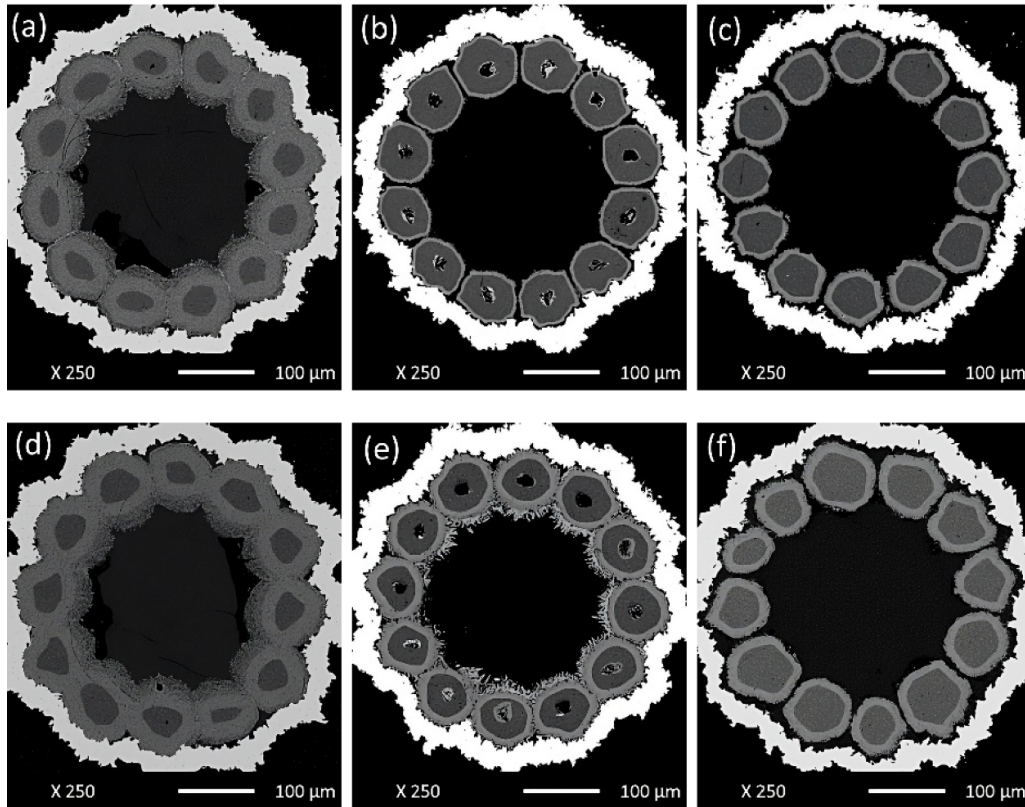
Figure 2. Back-scattered electron images of polished transverse cross-sections of wire samples after heat treatment: Hf-*noOS* (a), Hf-*coreOS* (b), Hf-*annularOS* (c), Zr-*noOS* (d), Zr-*coreOS* (e), Zr-*annularOS* (f).

Table 2. Summary of wire properties (elemental ratio in the cross-section of unreacted wires, filament size) and microstructure properties of reacted samples (fine-grained layer thickness and Nb$_3$Sn grain size). Elemental ratio is expressed relative to the total area inside the barrier (TOT), excluding barrier and external Cu. Standard deviations are given as a measure of the dispersion around the mean value.

Wire ID	Nb/Sn	Sn/Cu	Sn/TOT	Nb/TOT	Cu/TOT	Average filament size (μm)	Fine grains layer thickness (μm)	Long axis grain size (nm)	Short axis grain size (nm)
NbTa-*noOS*	1.22	1.45	0.34	0.42	0.23	76 ± 8	18 ± 3	119 ± 8	113 ± 9
Hf-*noOS*	1.55	1.53	0.31	0.49	0.20	89 ± 9	23 ± 2	120 ± 9	106 ± 8
Hf-*coreOS*	2.06	0.82	0.23	0.48	0.29	73 ± 3	04 ± 1	054 ± 6	040 ± 6
Hf-*annularOS*	1.44	1.00	0.29	0.42	0.29	67 ± 5	09 ± 2	060 ± 3	038 ± 5
Zr-*noOS*	1.68	1.63	0.30	0.51	0.19	90 ± 8	23 ± 3	112 ± 8	097 ± 5
Zr-*coreOS*	1.57	1.52	0.31	0.49	0.20	81 ± 3	13 ± 2	0072 ± 12	052 ± 9
Zr-*annularOS*	1.42	1.30	0.31	0.45	0.24	086 ± 11	10 ± 2	078 ± 6	057 ± 5

3. Results and discussion

Figure 2 shows polished transverse cross-sections after the reaction heat treatment of wire samples containing Hf (from 2.a to 2.c), and Zr (from 2.d to 2.f). Further information regarding our wires, including elemental area fraction in unreacted wires and fine grain layer thickness of the manufactured wires, is reported in table 2. The thickness of the fine-grained area (fine grains layer thickness in table 2, visible as the light grey annular region at the periphery of the reacted filaments in figure 2) varies from wire type to wire type, with a drastic reduction from ~20 μm to less than 10 μm when an OS is present. Considering a typical RIT wire developed for HL-LHC, whose final Nb filament size in a subelement is

approximately 1 μm and layer thickness is about 10 μm [11], we can argue that this important reduction of the diffusion kinetics in wires with an OS should not be a concern. However, further investigation in real scale multifilamentary wire will be necessary to make sure that the subelement can be fully reacted on a reasonable timescale.

Figure 3 shows representative images of the Nb$_3$Sn grains for each wire. As expected, the *noOS* wires prepared with Hf or Zr (figures 3(a) and (d)) exhibit large grains above 100 nm on both axes. Contrary to the findings of Balachandran *et al* [22] and Banno *et al* [23], our samples do not show grain refinement induced solely by the presence of Hf in the Nb alloy, as the grain size is consistent with that of commercially available Nb$_3$Sn wires and our own NbTa-*noOS* samples. The
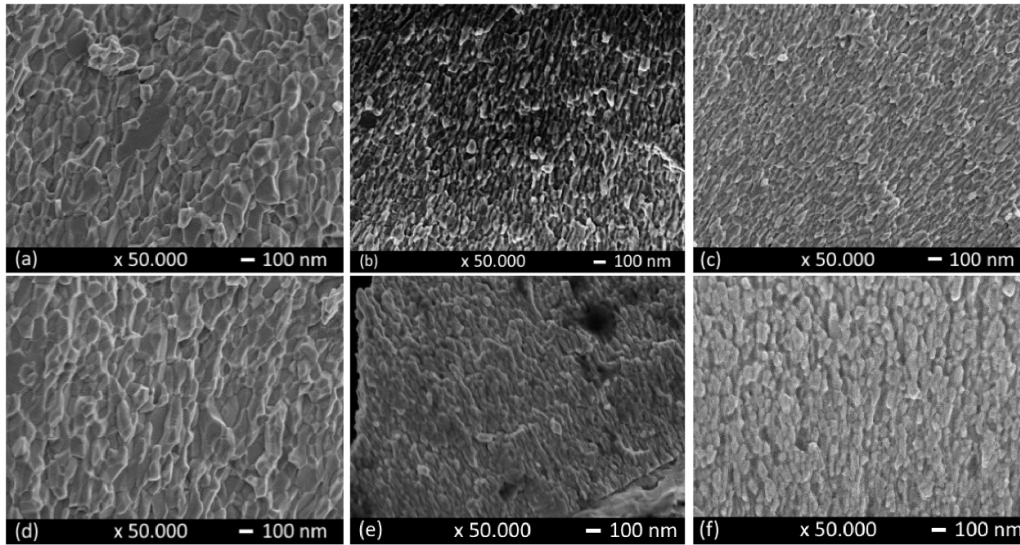
Figure 3. SEM images of fractured cross-section of Hf and Zr-containing wires: Hf*noOS* (a), Hf-*coreOS* (b), Hf-*annularOS* (c), Zr-*noOS* (d), Zr-*coreOS* (e), Zr-*annularOS* (f).

Hf-*coreOS* (figure 3(b)) and Hf-*annularOS* (figure 3(c)) wires exhibit a more elongated shape of the Nb_3Sn grain with respect to Hf-*noOS* wire as well as a pronounced reduction of the grain size. The mean size in the short axis direction was reduced to less than 40 nm for both of these wire types. Grain refinement was also observed in the Zr-containing samples when OS was added, with an elongated shape. However, for the Zr-containing Nb_3Sn, the effect of grain refinement induced by OS was less pronounced than that of the Hf-containing samples. Along the short axis, grains are refined down to 52 and 57 nm for Zr-*coreOS* and Zr-*annularOS* respectively. For both Hf and Zr samples, there is no significant difference in terms of grain refinement between the core and the annular placement of the OS.

At higher magnifications, brighter dots were observed on the exposed grains, as shown in figure 4. Based on previous observations and analyses [26, 35, 36], these dots are likely oxide nanoprecipitates (HfO_2 or ZrO_2, depending on the third element added to the Nb alloy). Currently we are not able to determine the composition or exact size of these particles. Based on these images, it would appear that these nanoparticles are mostly present at the grain boundaries, but it should be noted that the SEM images of the fractured samples reveal only oxide particles at the grain boundaries, leaving hidden oxide nanoparticles that may be present inside the grains. Transmission electron microscopy and atomic probe tomography performed by Xu *et al* [26, 37] have shown that, in average, there are more than ten oxide nanoparticles in each Nb_3Sn grain.

Samples containing an OS exhibited a significant improvement in layer J_c compared to *noOS* wires, as shown in figure 5. To underline the magnitude of the J_c enhancement, we added to the graph the layer J_c that would lead to a non-Cu J_c of 1500 A mm^{-2} (at 16 T, 4.2 K, the FCC target) in a wire with the same layer fraction of 60% of the non-Cu area as the high performance wires developed in the frame of the
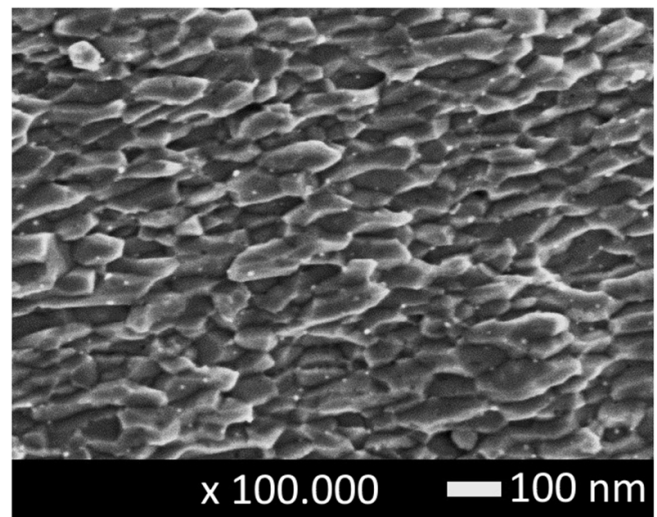

Figure 4. High magnification image of a fractured Hf-*coreOS* sample, showing oxide precipitates visible as bright spots.

HL-LHC project [2, 22]. This layer J_c amounts to an effective FCC layer target of 2500 A mm^{-2} at 16 T and 4.2 K. All the samples fabricated with an internal OS exhibit layer J_c values above this target. In particular, the Hf-*annularOS* wire exhibits a layer J_c of 3000 A mm^{-2} at 16 T and 4.2 K, while the samples containing Zr reach 2700 A mm^{-2}. While these J_c values are quite high compared with those in current state of the art Nb_3Sn wires without internally oxidized nanoparticles they are still well below the values exceeding 4000 A mm^{-2} that were measured by Xu *et al* [38] in PIT-APC Nb_3Sn wires based on Nb–Ta–Hf and Nb–Ta–Zr of the same nominal compositions as the alloys of our wires. The grain size distributions appearing comparable we can attribute this difference in J_c either to the distribution of the number concentration of the oxide nanoparticles and/or to distribution of more fundamental
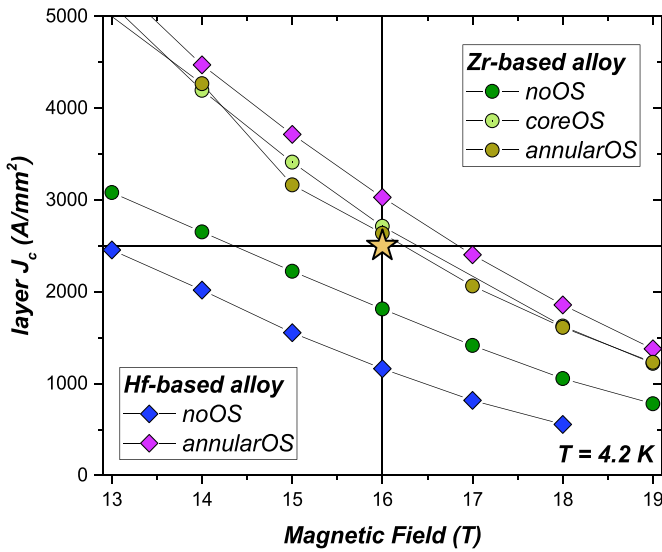
Figure 5. Layer J_c of the wire samples containing Hf or Zr, with and without OS. The star represents the FCC target as layer J_c in a wire having the same layer to non-Cu volume ratio as a HL-LHC RRP® wire.

Figure 6. B_{c2}(4.2 K) values of several samples of each wire calculated with different criteria (from top to bottom: 99%, 90%, 50%, 10% and 1%). Comparison with wire NbTa-*noOS*, fabricated with the same procedure using Nb-7.5 wt%Ta, is given.

properties like B_{c2}. We lack currently the technical means to characterize these distributions but we think that most of this difference comes from the gradient of the Sn content in the Nb$_3$Sn layer, which has a marked influence on B_{c2} distribution. We expect that RIT wires with internally oxidized nanoparticles and finer filaments heat treated to obtain lower composition gradients across the layer would also exceed the 4000 A mm^{-2} at 16 T and 4.2 K. In this context it is important to note that Xu *et al* [38] have also observed important differences between the J_c–s of wires based on the same alloy and same oxygen supply but different Nb/Sn ratios. As a further proof of the importance of other design parameters on the properties of the reacted layer we observe that because of the very thin Nb$_3$Sn layer (as shown in figure 2(b) and reported in table 2), the *coreOS* wire samples containing Hf did not have a sufficiently continuous layer of superconductor to allow current transport measurements.

The enhancement of J_c exhibited by the internally oxidized wires is not only due to grain refinement but also to a significant enhancement of B_{c2}. Figure 6 shows the ranges of B_{c2} values at different criteria as measured on multiple samples of each wire type. Experimental data show that B_{c2} (4.2 K) calculated using the 99% criterion increases to 29.2 and 29.3 T for Zr-*annularOS* and Hf-*annularOS* samples, respectively, as shown in figure 7. These values exceed by more than 1 T the B_{c2} value of 28 T for a sample fabricated with the same procedure and using Nb-7.5 wt%Ta alloy (NbTa-*noOS*). These results are in agreement with our previous measurements of mono-filamentary wires [20]. Considering the B_{c2}(99%), it can be seen that for both Hf- and Zr-containing samples, the introduction of OS enhances B_{c2} progressively from *coreOS* to *annularOS*. Zr-*noOS* did not show any B_{c2} enhancement with respect to the NbTa-*noOS* wire used as a reference, whereas the presence of Hf enhanced B_{c2} already without an OS. All our Zr-containing samples show a similar transition width,
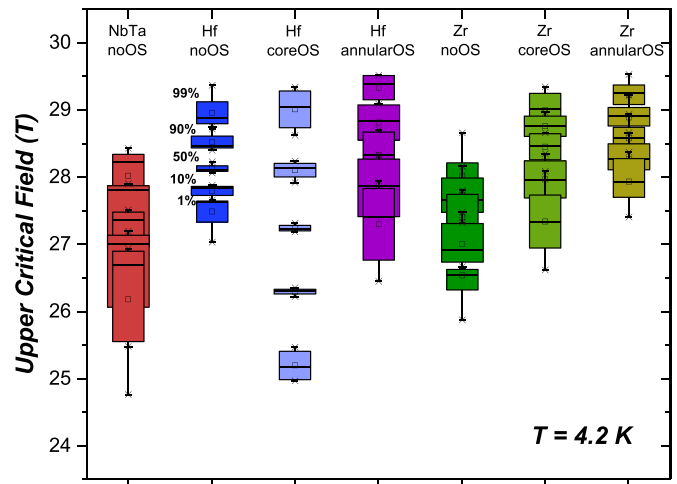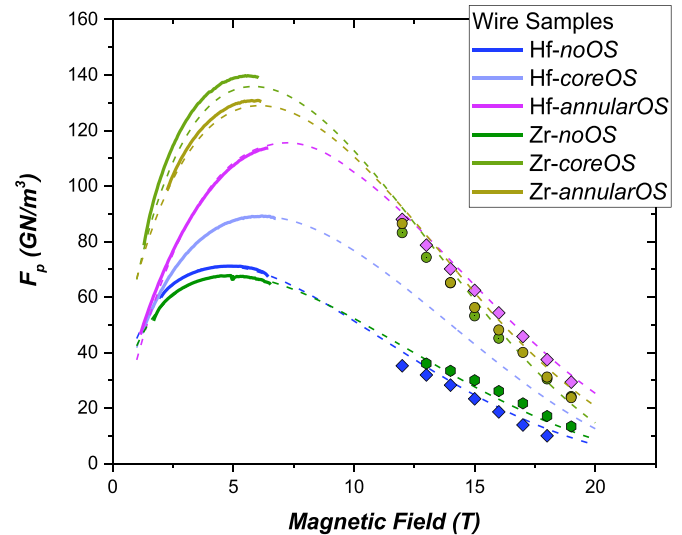

Figure 7. Pinning force as a function of magnetic field for Hf and Zr-containing samples, calculated from magnetic and transport layer J_c.

according to the difference between 99% and 1% criteria (i.e. B_{c2}(99%)–B_{c2}(1%)) reported in table 3, with no significant changes with introduction of OS. The Hf-containing samples exhibited higher variability with a wider transition width when OS was added.

These results confirm the enhancement of B_{c2} in the presence of Zr and OS reported in our previous work [20], and in the presence of Hf, as reported by Xu *et al* [18]. Thus far, a possible explanation given by Xu *et al* [37] argued that the presence of ZrO$_2$ (or HfO$_2$) leads to a higher Sn content in Nb$_3$Sn owing to the suppressed reaction rate at the Nb$_3$Sn/Nb alloy interface. A higher Sn concentration in Nb$_3$Sn, which is closer to stoichiometry, enhances B_{c2}. The reduced reaction layer observed in the cross-sections (figure 2) of the wires with an OS supports the explanation proposed by Xu *et al* [37].

Table 3. Average B_{c2} (99 and 1%) and F_p peak positions at 4.2 K.

Wire ID	Average B_{c2} (99%) (T)	Average B_{c2} (1%) (T)	$B/B_{c2}(1\%)$ at $F_p(max)$
NbTa-*noOS*	28.0	26.1	0.19
Hf-*noOS*	28.9	27.6	0.20
Hf-*coreOS*	29.0	25.1	0.24
Hf-*annularOS*	29.3	27.3	0.30
Zr-*noOS*	28.0	26.5	0.20
Zr-*coreOS*	29.0	27.3	0.22
Zr-*annularOS*	29.2	27.9	0.24

However, a more detailed investigation on the possible role of precipitates will be needed to understand their role in the B_{c2} enhancement, and if the same B_{c2} values will be observed in a real RIT wire with internal oxidation.

When an OS is added, a shift in the F_p peak ($F_p = J_c \times B$) to a higher absolute magnetic field is observed, as shown in figure 7, which shows the F_p curves calculated from both magnetic and transport measurements. The fits (dashed lines) were obtained using the B_{c2} (1%) in table 3 as a fixed parameter. This shift in the F_p peak is more substantial in the samples containing Hf, with the Hf-*annularOS* sample showing a peak at 7.3 T. The introduction of the OS also leads to an enhancement in the maximum value of F_p. At the peak, the Zr-containing samples with OS exhibits higher values of F_p of 140 and 130 GN m^{-3} for *coreOS* and *annularOS* respectively. Without OS, the Hf-containing sample exhibits a maximum F_p of 70 GN m^{-3}, which is progressively enhanced by the introduction of OS to 90 GN m^{-3} in the *coreOS* sample and to 135 GN m^{-3} in the *annularOS* sample. At a higher magnetic field, the Hf-*annularOS* sample takes over and exhibits the highest F_p at 16 T.

The shift of F_p peak is driven by the enhancement of B_{c2} as shown in figure 6, and by a modification of the pinning mechanism induced by the presence of HfO$_2$ and ZrO$_2$ precipitates. This can be observed by analyzing the normalized F_p as a function of reduced field ($b = B/B_{c2}(1\%)$) reported in figure 8.

Figure 8(a) shows the *normalized F_p* curves of the Hf-containing samples and figure 8(b) those of the Zr-containing samples, all calculated from the inductive $J_c(B)$ curves measured between 4.2 and 14 K. The magnetic field values were scaled to $B_{c2}(1\%)$ (as obtained from the $R(B)$ measurements) because this criterion gives a better scaling of the F_p, as compared with the 10% criterion. Wire samples without an OS display a peak of the normalized F_p at 0.2, as expected in the case of grain boundary pinning [39]. The introduction of the OS induces a shift in the F_p peak, which is more pronounced for the *annularOS* wires in both the Hf- and Zr-containing samples. The most significant shift of the peak is seen in the Hf-*annularOS* sample, with the peak occurring at 0.30 of the reduced field, which is attributable to an additional contribution to the pinning, from a different type of defect than the grain boundaries. An F_p peak at $b = 0.33$ can be associated with pinning by normal point defects [39]. The oxide nanoparticles are the obvious candidates for such pinning, and this is the chosen explanation given by Motowidlo *et al* [21],

Buehler *et al* [27] and Ortino *et al* [40]. In view of their results on samples reacted at low temperatures, with a particularly low average grain size of 30 nm and for which F_p maximized at $b = \sim 0.4$, Xu [9] concluded that instead of point pinning, individual pinning becomes important as the grain sizes approach the flux line spacing. If this were the actual additional pinning mechanism, a further reduction of the grain sizes would push the F_p peak towards the theoretical $b = 0.5$, a very interesting situation for high field applications. However, in more recent publications [24, 26], the same authors appear to favor the point defect pinning as an explanation for the shift of the F_p peak. A priori nothing excludes the possibility of three pinning contributions, but only further research will clear this issue. Moreover, based on the analysis of the change in the height of the F_p peak when passing from binary to Ta-doped Nb$_3$Sn, Ortino *et al* [40] cast doubt on the direct summation of grain boundary and point defect pinning.

In the absence of a clear understanding of the different pinning contribution, we can only enumerate and discuss the properties that may cause the difference observed between the positions of the F_p peaks of our Hf- and Zr-containing samples: the size distribution of the oxide precipitates, the spatial distribution of the oxide precipitates, the size distribution of the Nb$_3$Sn grains or a combination of some of these properties. Theoretical calculations show that the optimal size for flux pinning on insulating inclusions, like the oxide precipitates in these wires, is approximately twice the coherence length [41] of the superconductor. According to Xu *et al* [42], the element added to the Nb alloy has a significant influence on the oxide precipitate size (under the same heat treatment conditions), reporting that HfO$_2$ precipitates are smaller in size with respect to ZrO$_2$.

The grain refinement in Nb$_3$Sn with internally oxidized nanoparticles is due to the Zener drag effect [43], according to which the mobility of the grain boundaries, and thus the growth of the Nb$_3$Sn grain size, is reduced by the presence of small-sized precipitates, the resulting grain size being smaller for a low size and a high volume fraction of these precipitates. A high density of these precipitates can thus not only enhance the contribution to the pinning from the grain boundaries (finer grains imply a higher grain-boundary density) but also lead to a more important contribution to the vortex pinning from the nano-precipitates themselves, which results in a shift towards $b = 0.33$ of the F_p peak. Xu *et al* [42] show that the internal oxidation of Hf-containing samples produces larger effects on J_c compared to Zr, as HfO$_2$ ends up with a higher number concentration than ZrO$_2$ at the same solute atomic concentration in the starting Nb alloy, due to the smaller precipitate size of the HfO$_2$. The smaller size of the HfO$_2$ precipitates in comparison with ZrO$_2$ leads to a more effective Zener drag whereas the related higher number concentration tends to enhance the point defect pinning contribution. Comparing wires of the same atomic fraction of Hf and Zr (which is the case for Xu *et al* [42] and for us) and assuming complete internal oxidation of these species, the above considerations are experimentally supported by the smaller Nb$_3$Sn grains observed in Hf-containing samples compared to Zr-containing samples: Xu *et al* [42] observed Nb$_3$Sn grains of 53 nm and 64 nm in the
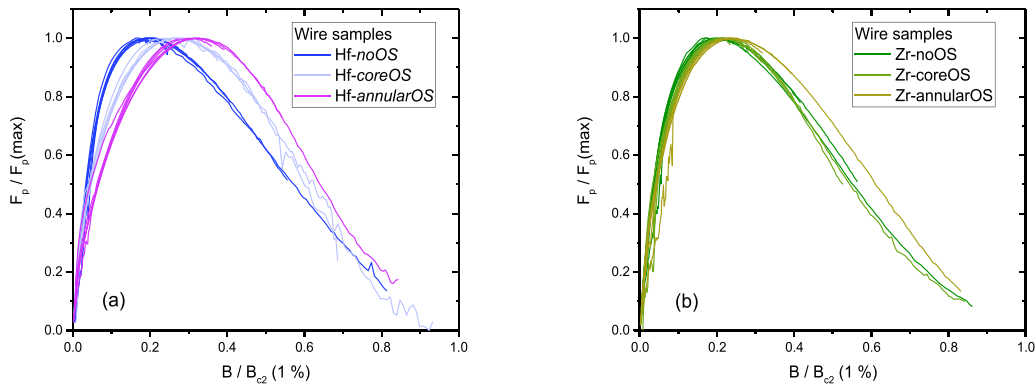
Figure 8. Normalized pinning force as a function of reduced field for Hf (a) and Zr-containing (b) samples. $B_{c2}(1\%)$ from $R(B)$ measurements is used to normalize the magnetic field.

outer boundaries for Hf and Zr samples (reacted at 675 °C), respectively, just as we observed smaller Nb_3Sn grain sizes in the Hf-containing samples with respect to the Zr-containing ones. However, in the absence of full characterizations of the size and spatial distributions we run the risk of looking at correlations rather than causalities. The F_p peak shift in our samples follows the same trend of higher values for HfO_2 but the peak values of F_p are less consistent. Unfortunately, other publications reporting measured dimensions of oxide precipitates do not allow fair comparisons as they are made on very different samples (manufacturing techniques, starting alloys and OS). They appear nevertheless to confirm a lower size for the HfO_2 precipitates. Based on atomic probe tomography, Tarantini *et al* [36] reported HfO_2 precipitate sizes of approximately 3 nm and Nb_3Sn grains below 70 nm (between 55 and 68 nm) in a wire manufactured by Balachandran *et al* [22] and reacted at 670 °C. Ortino *et al* [40] measured by transmission electron microscopy ZrO_2 precipitates of 4.6 nm and Nb_3Sn grain sizes of 70 nm in APC-PIT reacted at 675 °C. This comparison based on literature data and our own results in this paper is unfortunately not sufficient to fully understand how the size and distribution of oxides precipitate affect the grain refinement. Moreover, the variation of the size distributions of the Nb_3Sn grain across the reacted layer have rarely been systematically studied. One of these reports [21], shows not only significant grain size gradients but also broad size distributions. Investigations looking at the distributions of the precipitate size and precipitate position, and at the grain size vs position would be necessary to fully understand the influence of the precipitate particle size and number distributions on the grain refinement and ultimately on flux line pinning.

The present investigation shows that the placement of the OS influences the superconducting properties, but has a minimal impact on the grain refinement, as both approaches (core and annular) reduce the Nb_3Sn grain size to similar values for a given type of Nb alloy. The annular approach for introducing the OS yields better results in terms of B_{c2} enhancement and shift of the F_p peak position compared to the core approach. The *coreOS* samples have nevertheless significantly better properties than the wires manufactured without an OS,

underlining that an OS is essential for enhancing the high-field properties, whereas its placement enables optimization of the F_p and B_{c2}. The reasons for the different behaviors of the OS layouts are not yet clear but our future investigations will be aimed at determining whether they are related to different size and number distributions of the oxide nanoparticles resulting from different oxygen diffusion gradients.

4. Conclusions

We reported the successful implementation of the internal oxidation process on simple multi-filamentary wires manufactured through the RIT approach. Hf or Zr was added to the Nb alloy while SnO_2 was used as OS in two different configurations: core and annular. The introduction of the OS resulted in a refinement of the Nb_3Sn grains, which have a slightly elongated shape. In the wires with Hf and OS, the grain size was reduced to values below 40 nm on the short axis and below 60 nm on the long axis. Only a minor difference in grain size was observed between the *coreOS* and the *annularOS* layouts. In *Hf-annularOS* wires, the grain refinement produced an enhancement of the layer J_c up to 3000 A mm^{-2} at 16 T and 4.2 K. This value exceeds the layer J_c of 2500 A mm^{-2} necessary to achieve a non-Cu J_c of 1500 A mm^{-2} (at 16 T, 4.2 K, the FCC target) in a wire having the same layer fraction as the high-performance wires developed for the HL-LHC project. The Hf or Zr oxide precipitates not only inhibit the grain growth during the heat treatment but also appear to act as effective pinning centers, causing a shift in the pinning force peak to higher reduced fields. This shift is more pronounced when SnO_2 is added in the *annularOS* configuration, and for the Hf-containing samples. Indeed, the *Hf-annularOS* sample shows an F_p peak at a field value corresponding to 0.3 B_{c2}. The introduction of OS resulted in $B_{c2}(99\%, 4.2 K)$ values of 29.2 and 29.3 T for Zr and Hf-*annularOS* samples respectively. These values are approximately 1.3 T higher than those of a wire manufactured with a Nb–Ta alloy, which was used as a reference. The mechanism behind the enhancement of B_{c2} and the different impact of the *coreOS* and *annularOS*

approaches on the F_p-peak shift are not fully understood and deserve dedicated investigations. On a general perspective, this work presents a promising approach to introduce a powder OS in a simplified RIT wire. This is a first step towards the introduction of an OS in the layout of the subelement of practical RIT wires, which presents difficulties related to the fine size of the filaments in the final wires and to the need for a uniformly distributed OS that does not affect negatively the fabrication of the wire. In this study, we examined the annularOS and the coreOS configurations, given their previous use in other works [18, 20]. However, alternative OS configurations will probably be more suitable for RIT wires. In our forthcoming research, we will explore various methods for incorporating an OS into full-scale RIT subelements and examine their effect on deformability and superconducting properties. This is currently the major technological challenge for integrating internal oxidation into RIT wires. Given that a winning solution has not been yet identified, it is too early to evaluate how significantly this will increase the conductor cost but it is fairly clear that the additional manufacturing steps could bring it closer to the cost of the PIT-type Nb_3Sn superconductors. The fabrication of PIT-APC Nb_3Sn wires is uniquely suitable for the introduction of an OS but we think that continued research and development on both RIT and PIT-APC Nb_3Sn wires is the best way to ensure the availability of suitable conductors for future large scale projects like FCC.

Data availability statement

The data that support the findings of this study are openly available at the following URL/DOI: Data will be available upon request.

Acknowledgments

ORCID iDs

G Bovone ⓘ https://orcid.org/0000-0002-9161-7828
F Buta ⓘ https://orcid.org/0000-0002-7119-8427
T Bagni ⓘ https://orcid.org/0000-0001-8654-783X
M Bonura ⓘ https://orcid.org/0000-0002-8512-0989
C Senatore ⓘ https://orcid.org/0000-0002-9191-5016

References

[1] Apollinari G *et al* High-luminosity Large Hadron Collider (HL-LHC) (Accessed 16 June 2022) (https://doi.org/10.23731/CYRM-2017-004)

[2] Ferracin P *et al* 2016 Development of MQXF: the Nb_3Sn low-β quadrupole for the HiLumi LHC *IEEE Trans. Appl. Supercond.* **26** 4–10

[3] Abada A *et al* 2019 FCC-hh: the hadron collider *Eur. Phys. J.* **228** 755–1107

[4] Tommasini D *et al* 2019 The 16 T dipole development program for FCC and HE-LHC *IEEE Trans. Appl. Supercond.* **29** 1

[5] Ballarino A *et al* 2019 The CERN FCC conductor development program: a worldwide effort for the future generation of high-field magnets *IEEE Trans. Appl. Supercond.* **29** 1–9

[6] de Marzi G *et al* 2022 Magnetic and electromechanical characterization of a high-JCRRP wire for the HL-LHC MQXF cable *IEEE Trans. Appl. Supercond.* **32** 1–5

[7] Parrell J A 2004 Nb_3Sn conductor development for fusion and particle accelerator applications *AIP Conf. Proc.* **711** 369–75

[8] Parrell J A, Zhang Y, Field M B, Cisek P and Hong S 2003 High field Nb_3Sn conductor development at Oxford superconducting technology *IEEE Trans. Appl. Supercond.* **13** 3470–3

[9] Xu X 2017 A review and prospects for Nb_3Sn superconductor development *Supercond. Sci. Technol.* **30** 093001

[10] Barzi E, Bossert M, Field M, Li P, Miao H, Parrell J, Turrioni D and Zlobin A V 2017 Heat treatment optimization of Rutherford cables for a 15-T Nb_3Sn dipole demonstrator *IEEE Trans. Appl. Supercond.* **27** 1–5

[11] Sanabria C, Field M, Lee P J, Miao H, Parrell J and Larbalestier D C 2018 Controlling Cu-Sn mixing so as to enable higher critical current densities in RRP ® Nb_3Sn wires

[12] Godeke A, den Ouden A, Nijhuis A and ten Kate H H J 2008 State of the art powder-in-tube niobium-tin superconductors *Cryogenics* **48** 308–16

[13] Boutboul T, Oberli L, den Ouden A, Pedrini D, Seeber B and Volpini G 2009 Heat treatment optimization studies on PIT Nb_3Sn strand for the NED project *IEEE Trans. Appl. Supercond.* **19** 2564–7

[14] Xu X, Sumption M D and Collings E W 2014 Influence of heat treatment temperature and Ti doping on low-field flux jumping and stability in $(Nb-Ta)_3Sn$ strands *Supercond. Sci. Technol.* **27** 095009

[15] Schauer W and Schelb W 1981 Improvement of Nb_3Sn high field critical current by a two-stage reaction *IEEE Trans. Magn.* **17** 374–7

[16] Benz M G 1968 The superconducting performance of diffusion-processed $Nb_3Sn(Cb_3Sn)$ doped with ZrO_2 particles *Trans. Metall. Soc. AIME* **242** 1067–70

[17] Zeitlin B A, Gregory E, Marte J, Benz M, Pyon T, Scanlan R and Dietderich D 2005 Results on mono element internal tin Nb_3Sn conductors (MBIT) with Nb7.5Ta and Nb(1Zr + Ox) filaments *IEEE Trans. Appl. Supercond.* **15** 3393–8

[18] Xu X, Sumption M, Peng X and Collings E W 2014 Refinement of Nb_3Sn grain size by the generation of ZrO_2 precipitates in Nb_3Sn wires *Appl. Phys. Lett.* **104** 082602

[19] Buta F *et al* 2018 Properties and microstructure of binary and ternary Nb_3Sn superconductors with internally oxidized ZrO_2 nanoparticles *Applied Superconductivity Conf.* (*Seattle, USA*) pp 1MPo2A–06

[20] Buta F, Bonura M, Matera D, Bovone G, Ballarino A, Hopkins S C, Bordini B, Chaud X and Senatore C 2021 Very high upper critical fields and enhanced critical current densities in Nb_3Sn superconductors based on Nb–Ta–Zr alloys and internal oxidation *J. Phys. Mater.* **4** 025003

[21] Motowidlo L R, Lee P J, Tarantini C, Balachandran S, Ghosh A K and Larbalestier D C 2018 An intermetallic powder-in-tube approach to increased flux-pinning in Nb_3Sn by internal oxidation of Zr *Supercond. Sci. Technol.* **31** 014002

[22] Balachandran S, Tarantini C, Lee P J, Kametani F, Su Y-F, Walker B, Starch W L and Larbalestier D C 2019 Beneficial influence of Hf and Zr additions to $Nb_4at\%Ta$ on the vortex pinning of Nb_3Sn with and without an O source *Supercond. Sci. Technol.* **32** 044006

[23] Banno N, Morita T, Yagai T and Nimori S 2021 Influence of parent Nb-alloy grain morphology on the layer formation of Nb_3Sn and its flux pinning characteristics *Scr. Mater.* **199** 113822

[24] Xu X, Rochester J, Peng X, Sumption M and Tomsic M 2019 Ternary Nb_3Sn superconductors with artificial pinning centers and high upper critical fields *Supercond. Sci. Technol.* **32** 02LT01

[25] Drost E, Specking W and Flükiger R 1985 Comparison of superconducting properties and residual resistivities of bronze processed Nb_3Sn wires with Ta, Ti and Ni+Zn additives *IEEE Trans. Magn.* **21** 4–7

[26] Xu X, Peng X, Rochester J, Lee J and Sumption M 2020 High critical current density in internally-oxidized Nb_3Sn superconductors and its origin *Scr. Mater.* **186** 317–20

[27] Buehler C *et al* 2020 Challenges and perspectives of the phase formation of internally oxidized PIT-type Nb_3Sn conductors *IEEE Trans. Appl. Supercond.* **30** 1–5

[28] Weber I, Longo E and Leite E 2000 $SnO_2 \cdot Nb_2O_5$ films for ethanol sensor, obtained by deposition of alcoholic suspensions *Mater. Lett.* **43** 166–9

[29] Landolt D 1987 Review fundamental aspects article of electropolishing *Electrochim. Acta* **32** 1–11

[30] Bean C 1964 Magnetization of high field superconductors *Rev. Mod. Phys.* **36** 31–39

[31] Eikelboom J A, Hartmann R A, Van L J M and Klundert D E 1989 Hysteresis losses in hollow superconductors *IEEE Trans. Magn.* **25** 1968–71

[32] Eikelboom J A and van de Klundert L J M 1991 Hysteresis losses in hollow superconducting filaments and in multifilament systems *Cryogenics* **31** 354–62

[33] Kim Y B, Hempsteadp C F and Strnad A R 1963 Magnetization and critical supercurrents *Phys. Rev.* **129** 528–35

[34] Matera D, Bonura M, Černý R, McKeown Walker S, Buta F, LeBoeuf D, Chaud X, Giannini E and Senatore C 2020 High-field superconductivity in C-doped MgB_2 bulk samples prepared by a rapid synthesis route *Sci. Rep.* **10** 1–16

[35] Xu X, Sumption M D and Peng X 2015 Internally oxidized Nb_3Sn strands with fine grain size and high critical current density *Adv. Mater.* **27** 1346–50

[36] Tarantini C, Kametani F, Balachandran S, Heald S M, Wheatley L, Grovenor C R M, Moody M P, Su Y-F, Lee P J and Larbalestier D C 2021 Origin of the enhanced Nb_3Sn performance by combined Hf and Ta doping *Sci. Rep.* **11** 1–8

[37] Xu X, Sumption M D, Lee J, Rochester J and Peng X 2020 Persistent compositions of non-stoichiometric compounds with low bulk diffusivity: a theory and application to Nb_3Sn superconductors *J. Alloys Compd.* **845** 156182

[38] Xu X, Peng X, Wan F, Rochester J, Bradford G, Jaroszynski J and Sumption M 2023 APC Nb_3Sn superconductors based on internal oxidation of Nb-Ta-Hf alloys *Supercond. Sci. Technol.* **36** 035012

[39] Dew-Hughes D 1974 Flux pinning mechanisms in type II superconductors *Phil. Mag.* **30** 293–305

[40] Ortino M, Pfeiffer S, Baumgartner T, Sumption M, Bernardi J, Xu X and Eisterer M 2021 Evolution of the superconducting properties from binary to ternary APC-Nb_3Sn wires *Supercond. Sci. Technol.* **34** 035028

[41] Takezawa N and Fukushima K 1997 Optimal size of an insulating inclusion acting as a pinning center for magnetic flux in superconductors: calculation of pinning force *Physica* C **290** 31–37

[42] Xu X, Peng X, Rochester J, Sumption M D, Lee J, Calderon Ortiz G A and Hwang J 2021 The strong influence of Ti, Zr, Hf solutes and their oxidation on microstructure and performance of Nb_3Sn superconductors *J. Alloys Compd.* **857** 158270

[43] Ryum N, Hunderi O and Nes E 1983 On grain boundary drag from second phase particles *Scr. Metall.* **17** 1281–3